Communication

Asymmetric Dual-Grating Dielectric Laser Accelerator Optimization

Sophie Crisp * , Alexander Ody and Pietro Musumeci

Department of Physics and Astronomy, University of California, Los Angeles, CA 90095, USA
* Correspondence: sophiecrisp@physics.ucla.edu

Abstract: Although hundreds of keV in energy gain have already been demonstrated in dielectric laser accelerators (DLAs), the challenge of creating structures that can confine electrons for multiple millimeters remains. We focus here on dual gratings with single-sided drive, which have experimentally demonstrated energy modulation numerous times. Using a Finite-Difference Time-Domain simulation to find the fields within various DLA structures and correlating these results with particle tracking simulation, we look at the impact of teeth height and width, as well as gap and offset, on the performance of these structures. We find a tradeoff between electron throughput and acceleration; however, we also find that for any given grating geometry, there is a gap and offset that will allow some charge acceleration. For our 780 nm laser wavelength, this results in a 1200 nm optimal gap size for most gratings.

Keywords: DLA; particle accelerators; lasers

1. Introduction

Dielectric laser accelerators could allow for the proliferation of accelerator devices throughout small laboratory and medical settings. Enabled by materials advancement and power-efficient laser technology, DLAs have produced GeV/m gradients and >700 μm interaction lengths [1,2]. However, energy gain has been limited to 300 keV, in part by the difficulty of manufacturing long structures with sub-micron gap sizes. Many structures have been proposed, but dual grating structures remain useful for their simplicity and tunability [3–7].

Prior optimization works have limited themselves primarily to gaps less than the illumination wavelength, λ [8–12]. However, for experimental demonstrations of long interactions, there is a major reason one might want to increase that gap size: increasing charge throughput. In addition, there remain challenges with the manufacture of bonded structures of multi-mm scale, which prohibits the setting of one particular gap size. Instead, a mounting scheme for dual gratings has been developed, which allows for far more flexibility in structure parameters, even during the experiment [13]. This drives the analysis of structures with gratings aligned to non-zero offsets and larger than wavelength gap size.

In this paper, we will first examine the field structure within a standard single-drive dual-grating structure. Combining this with particle tracking simulations will allow us to determine goal parameters. Thus, we approach the problem of grating geometry sequentially; first, by finding the highest-efficiency geometry for the grating far from the incident laser (i.e., the right grating), and then scanning over geometries for the left grating. The tradeoff between acceleration and throughput will be discussed in detail, as it drives the optimization of structure parameters. By changing the gap and offset of the structure, we will analyse the expected energy gain and electron throughput of the designed double grating structure.

2. Materials and Methods

We begin by examining the field structure created in the single drive dual grating structure geometry, shown in Figure 1. Single drive refers to a laser pulse incident on one

side of the structure; dual grating refers to the two transmission gratings that are are used to form the structure. The gratings have a gap between them through which an electron beam can pass. Opposing grating teeth may have some offset between them; prior work has referred to 'gliding' the teeth across one another [14]. The laser propagates in the y-direction, polarized parallel to the propagation of the electrons (z) with velocity $v = \beta c$. The x-direction is assumed to be semi-infinite such that the laser excites a TM mode in the structure. One can describe the longitudinal component of the nth order mode in a DLA by the real part of

$$E_{n,z} = iE_0 \left(d_n e^{-\Gamma_n y} + c_n e^{\Gamma_n y} \right) e^{i(k_n z - \omega_0 t)}. \tag{1}$$
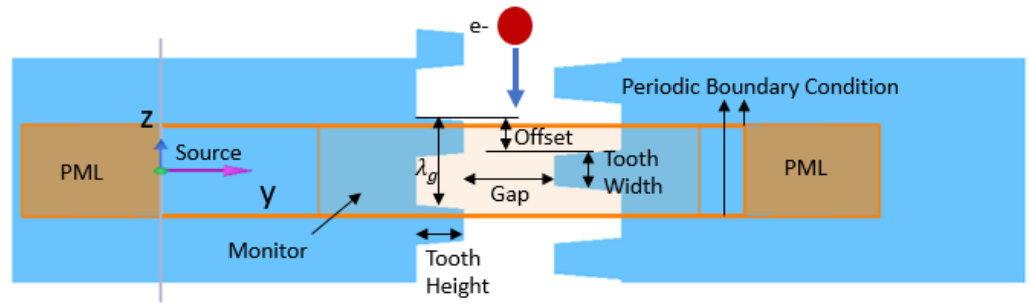

Figure 1. Dual grating simulation setup in Lumerical. The source is a 780 nm plane wave at normal incidence, originating from within the structure, since reflection at the surface will be unchanged for each structure. The simulation substrate is 3 μm thick (y); increasing this thickness does not change simulation outputs. The interior shaded orange section is meshed with a 5 nm step. A monitor records all components of the electric and magnetic fields as a function of y, z, and ω_0. The teeth are tapered to reflect realistic etching capabilities.

The laser has angular frequency ω_0 and amplitude E_0. The complex coefficients d_n and c_n are dimensionless and describe the amplitude of the evanescent wave near the walls of the grating structure. Since the laser propagates orthogonal to the structure, there is no additional wavenumber in the beam direction (k_z) component. Each Γ_n must satisfy the dispersion relation

$$k_n^2 - \Gamma_n^2 = k_0^2. \tag{2}$$

In order to satisfy the resonant phase condition, $\beta k_n = k_0$; it follows that the fields of interest are evanescent with decay length Γ_n. As a result, gap sizes with large acceleration fields are restricted to the order of a laser wavelength. As the only free parameters in Equation (1), c_n and d_n alone may be used to parameterize the DLA. However, it is useful to define some additional quantities to understand accelerating and deflecting modes. As in Dylan et al. [14], we define the parameter r_n as

$$r_n = c_n/d_n = |r_n| e^{i\phi_{r_n}}. \tag{3}$$

It can be useful to think not only in terms of $|r_n|$, but instead in terms of the location of the potential minimum in the structure, y_c, labeled in Figure 2. We calculate the location of the minimum of $|E_{n=1,z}|$ to be $y_c = -\ln(|r|)/(2\Gamma)$ and define the effective gap as twice the distance from y_c to the nearest grating wall. We now drop the subscript n, as only the $n = 1$ mode matches the accelerated electrons; for example the matched $\phi_{r_{n=1}}$ is simply ϕ. Finally, we define the structure factor

$$\kappa = |d e^{-\Gamma y_c} + c e^{\Gamma y_c}| \tag{4}$$

and note that this definition agrees with prior definitions where the accelerating gradient is equal to κE_0 when the phase velocity of the mode matches the electron velocity.
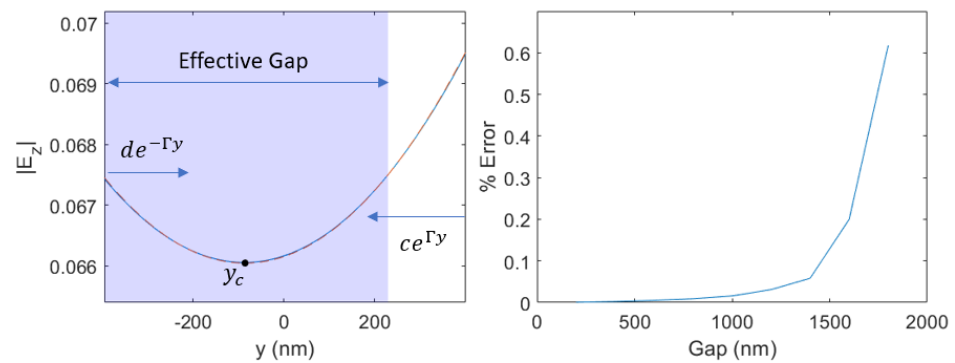
Figure 2. At left, an example of the average phase-matched field from Lumerical and the retrieved fit for a structure with 800 nm gap, left tooth height of 150 nm, right tooth height of 650 nm, and 390 nm tooth width. The offset here was −300 nm to maximize the effective gap. At right, the percent error of the retrieved fit compared to the simulated field is shown as a function of gap size. For gaps under 1600 nm, the fitted c_1 and d_1 match the actual fields curvature to within 0.1% error.

When the relative amplitudes of the counterpropagating waves are equal, as would be the case in a symmetric dual illuminated structure, $r = 1$ and $y_c = 0$. In this case, when the relative phase $\phi = 0$, a symmetric accelerating cosh-like mode is formed around the center of the gap. Conversely, when $\phi = \pi/2$ a deflecting sinh mode is created. Since our focus is in creating accelerators with high accelerating gradients and high throughput, it is clear that ϕ must be kept close to 0 in order to avoid deflecting the majority of electrons.

To better quantify this, we measure throughput of particles in a toy structure using a spatial harmonics-based simulation (SHarD), which is explained at length by Ody et al. [15]. For the illumination, we assume a Gaussian laser pulse with a peak field of 1 GV/m and σ_z of 5 mm to be incident on a 5 mm, 780 nm periodicity structure with an 800 nm gap. A total of 1000 electrons are initialized with 6 MeV energy, 0.1 nm emittance and are uniformly spaced within a grating period. There is no Alternating Phase Focusing [16,17] or ponderomotive-based focusing [18] scheme, but the laser field phase is tapered to match the energy gain of the accelerated electrons. In practice, this tapering could be accomplished via soft-tuning the laser phase with a spatial light modulator (SLM); although, so far this has not been experimentally demonstrated [15,19]. Without an incident field, 99.3% of particles are transmitted; this drops to 57.2% with the addition of an input field. Since the electrons sample every injection phase, many lose energy throughout the structure. We therefore define a 'captured' particle to be one where the particle's final Lorentz factor, γ, is larger than 95% of γ_{res}, where γ_{res} is the Lorentz factor of the resonant particle after acceleration. We use the number of captured particles as the figure of merit.

Figure 3 shows the result of varying r and ϕ in this toy structure while keeping the structure factor constant. If one considers a dual-drive experiment, with simultaneous illumination on both sides of the structure, there is a clear design target with $y_c = 0$ and $\phi = 0$. However, implementing a single-sided drive (and dual grating) means one must instead balance capture rates with structure factor. From the toy model we gather that at the least, y_c must be located within the structure gap ($r > 0.6$), and ϕ kept to below 0.2 radians.

From here, we assert that the ideal accelerating structure would have maximal structure factor, maximal effective gap, and ϕ close to zero. Because it is not possible to both maximize κ and minimize y_c and ϕ, we instead seek to understand the relation between structure geometries and these parameters such that an adequate middle ground is reached.
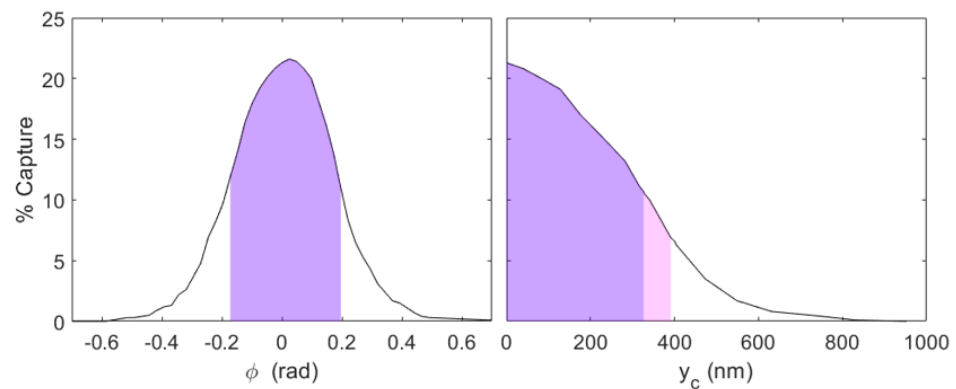
Figure 3. Simulations with dummy parameters show that less symmetric structures capture fewer particles. These 5 mm-long structures have an 800 nm gap and $\kappa = 0.2$. At left, r is kept at 1 and ϕ varied. At right, $\phi = 0$ and r, varied, which equates to moving y_c across the structure gap. Highlighted in purple are the parameters for which >50% of the symmetric case capture rate is obtained. The pink extension refers to structures for which the effective gap is greater than 0 nm, but the capture does not meet the 50% threshold. We conclude that for effective capture, y_c must be within the physical gap, and $|\phi|$ must be less than 0.2.

3. Results

The Finite-Difference Time-Domain simulation software Lumerical 2021 R2.3 is used in order to simulate fields within the grating structures. A plane wave source is injected orthogonal to the DLA structure. The teeth are defined with a 10deg taper, in accordance with etching capabilities (although this does not significantly affect parameters). Upon transmission through the structure, a perfectly matched layer (PML) eliminates extraneous reflections in y. The structure is assumed perfectly periodic (and infinite) in z, so a periodic boundary condition is used. Fused silica with a refractive index of 1.45 is used, due to its high damage threshold and commercial availability.

A frequency domain monitor is used to retrieve the electric field throughout the structure gap and Fourier transformed to phase-velocity match a 6 MeV electron. We can fit Equation (1) using $\Gamma = k_0/(\beta\gamma)$, as shown in Figure 2 example.

Although the fields are defined by only c_n and d_n, they are controlled by a number of input parameters. For these dual grating structures, the teeth height, teeth width, gap, and offset are all controllable parameters. Of these, teeth height and teeth width are intrinsic to the manufactured grating; gap and offset can in principle be controlled in assembly. To verify our simulations, we inputted the parameters for the Peralta structure, a well-studied symmetric structure that has been used for many relativistic dual grating DLA experiments [1,20]. We found a structure factor of 0.24, in agreement with previous calculations [2,9].

For the initial simulations, the gratings on top and bottom were identical—we will refer to these as symmetric structures, regardless of offset. The gap size is 800 nm; smaller gaps result in very low transmission, which make them unrealistic target structures for near-term experiments. The tooth width is set to a 50% duty cycle, 390 nm. Then tooth height was scanned over from 300 nm to 900 nm. Figure 4 shows the results of this scan; the maximum at 650 nm in tooth height shows the best geometry for the right grating. Following this, a scan over tooth width from 200 nm to 600 nm was conducted, again with symmetric structures (with teeth height set to 650 nm); the optimal width is 425 nm, or 54% duty cycle. We ultimately have a manufacturing constraint of <390 nm toothwidth, so subsequent simulations use that.

From these scans, a baseline optimal grating for maximal structure factor is found. As was previously discussed, however, this analysis ignores the very significant impact of asymmetric fields within the structure for the single-drive case. We therefore move on to structures with asymmetric tooth height.
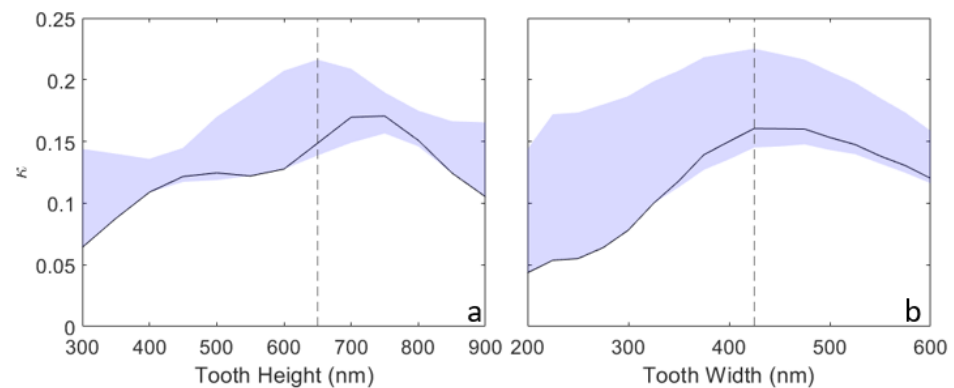
Figure 4. The structure factor fits for a symmetric structure with an 800 nm gap and a 50% duty cycle. In (**a**), grating offset is scanned over for each tooth height to retrieve maximum and minimum κ for each potential structure, shaded in blue. The black outline represents the offset = 0 case. There is a clear maximum in potential κ at 650 nm tooth height, highlighted by the dashed lined. In (**b**), a symmetric 650 nm tooth height structure is scanned over tooth width. A maxima is found for a 425 nm tooth width, although the structure is seen to be less sensitive to width than height.

It is informative to look at how the gap and offset impact the retrieved ϕ and r. Figure 5 shows this relation for the structure with a left tooth height of 450 nm. For these gratings, gaps larger than 800 nm allow $|\phi|$ to be close to zero. Due to the deflecting forces for nonzero ϕ, this means that shrinking the gap size to optimize the structure factor would be ineffective in improving the DLA.
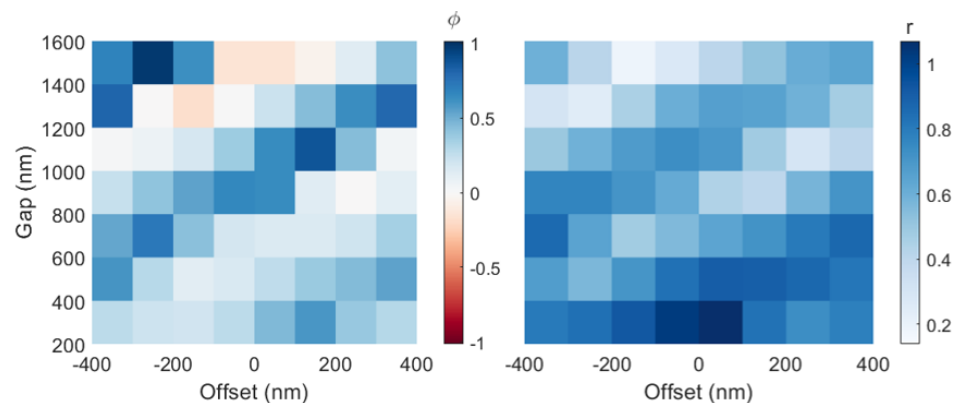

Figure 5. The retrieved ϕ (**left**) and r (**right**) for an asymmetric structure with left tooth height of 450 nm and right tooth height of 650 nm. The tooth width for both gratings is 390 nm. For certain combinations of gap and offset, ϕ may be set to 0; in this case, only gaps ≥ 800 nm have this capability. r generally decreases with increasing gap size, and has a similar periodic variation with offset as ϕ.

Seeking to find the optimal combination of asymmetric grating geometries, we conduct an additional parameter scan. The right grating is set with 390 nm tooth width and 650 nm tooth height. We then vary the left grating tooth height, while letting the offset and gap size change. Because small $|\phi|$ is critical to minimizing the sinh deflection mode, in Figure 6, we plot only the gap-offset combinations that obey a $|\phi| < 0.2$ rad criterion. The resulting upper-right boundary is the Pareto front. We are using effective gap here as a proxy for particle capture; although, there is certainly interplay between the acceptance space of $|\phi|$ and $|r|$.

Looking at the left side of Figure 6, one finds a large number of structure parameters that result in a 0 nm effective gap. These structures would, given a long enough laser interaction, result in all electrons being thrown into the grating walls. In general, a larger left tooth height, bringing the structure closer to symmetric, results in a smaller effective gap However, it also results in a larger structure factor, as evidenced by the red-to-blue

gradient, which crosses from left to right. One set of points does not follow this trend: the darkest-blue points corresponding to 50 nm teeth are obvious outliers on the bottom of the plot. Here, the structure factor is lowest due to the inefficiency of the left grating, and y_c is moved so far to the left that the effective gap is lower than structures with higher κ.
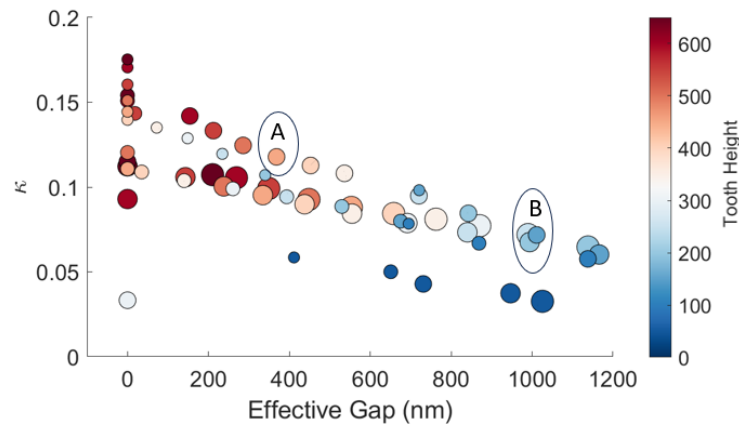

Figure 6. Simulations scan over offset, gap, and left tooth height fit c_1 and d_1 parameters, from which κ and the effective gap are calculated. Each point corresponds to an offset that minimizes $|\phi|$ for that particular gap and tooth height combination. Only points which satisfy $|\phi| < 0.2$ rad are plotted. Points are colored according to tooth width, shown on the colorbar and are sized by the absolute gap size, from 800 nm to 1600 nm in 200 nm steps. Higher tooth heights correspond to higher κ values. One can take the upper-right boundary to be the Pareto front. Point A denotes the target geometry. The points enclosed in B denote a region of interest, if a lower structure factor is permissible, where the absolute gap is more comparable to the effective gap.

For the symmetric structure (left tooth height = 650 nm,) only the 1600 nm gap has an effective gap larger than 0 nm. However, this lands the structure well under the Pareto front. In fact, it appears that the Pareto front is mostly composed of 1200 nm gap structures. Further study would be needed to find the proportionality of this to structure periodicity. Unfortunately, the Pareto front for grating selection consists of different gratings, making it impossible to select a single structure and adjust its gap and offset to access different regions of this front.

One vital consideration for structure selection is absolute gap size; the larger the gap, the easier the assembly. A case could therefore be made for looking toward the right of Figure 6, where clusters of points have different grating heights and absolute gap sizes, but very similar effective gaps and structure factors. For example, one can maintain an approximate effective gap of 1 um with an absolute gap size from 1200 to 1600 nm without further sacrificing structure factor by selecting a left tooth height of 250 nm (labeled cluster B).

We choose, however, to prioritize structure factor more highly, and so focus our attention on the point labelled A. This has an absolute gap size of 1200 nm, effective gap of 368 nm, $|\phi| = 0.0143$, and $\kappa = 0.118$. This is produced by an offset of -100 nm. This structure factor should allow for the target of 1 MeV acceleration in the 5 mm structure to be met with <2 GV/m of incident field, within the bounds of prior experiments.

4. Discussion

We have examined the optimization for a single-drive dual-grating dielectric laser accelerator structure. We find that by varying the teeth height and width of the gratings, we may modify the peak structure factor and effective gap. Only a small subset of gap and offset combinations will minimize the relative phase $|\phi|$, which is required for an accelerating mode.

We conclude that for our $\lambda_0 = 780$ nm, single-side-illuminated dual-grating structure, the optimal gap size is 1200 nm, far from the $\lambda_0/4$ criterion, which maximizes κ. If all possible gap sizes and offsets are available (as they generally are when using slab gratings), any tooth height could give rise to an effective gap larger than zero as well while having a near zero ϕ. However, this is at the expense of the structure factor.

This analysis is critical for understanding the expected accelerated population from a given DLA. Since sub-micron gap sizes inherently limit charge throughput, care must be taken to assemble structures with a balance between the acceleration gradient and the effective gap. Using simple unchirped gratings like these reduces cost while allowing for soft-tuning approaches like laser phase tapering to address dynamic effects from longer interactions [19].

Author Contributions: Conceptualization, P.M. and S.C.; methodology, A.O. and S.C.; software, S.C. and A.O.; validation, S.C. and A.O.; formal analysis, S.C.; investigation, S.C.; resources, P.M.; data curation, S.C. and A.O.; writing—original draft preparation, S.C.; writing—review and editing, S.C., A.O. and P.M.; visualization, S.C.; supervision, P.M.; project administration, P.M.; funding acquisition, P.M. All authors have read and agreed to the published version of the manuscript.

Data Availability Statement: The data presented in this study are available on request from the corresponding author.

Conflicts of Interest: The authors declare no conflict of interest.

References

1.　Cesar, D.; Maxson, J.; Shen, X.; Wootton, K.P.; Tan, S.; England, R.J.; Musumeci, P. Enhanced energy gain in a dielectric laser accelerator using a tilted pulse front laser. *Opt. Express* **2018**, *26*, 29216–29224. [CrossRef] [PubMed]

2.　Cesar, D.; Custodio, S.; Maxson, J.; Musumeci, P.; Shen, X.; Threlkeld, E.; England, R.J.; Hanuka, A.; Makasyuk, I.V.; Peralta, E.A.; et al. High-field nonlinear optical response and phase control in a dielectric laser accelerator. *Commun. Phys.* **2018**, *1*, 1–7. [CrossRef]

3.　England, R.J.; Noble, R.J.; Bane, K.; Dowell, D.H.; Ng, C.K.; Spencer, J.E.; Tantawi, S.; Wu, Z.; Byer, R.L.; Peralta, E.; et al. Dielectric laser accelerators. *Rev. Mod. Phys.* **2014**, *86*, 1337–1389. [CrossRef]

4.　Chang, C.M.; Solgaard, O. Silicon buried gratings for dielectric laser electron accelerators. *Appl. Phys. Lett.* **2014**, *104*, 184102. [CrossRef]

5.　Wu, Z.; England, R.J.; Ng, C.K.; Cowan, B.; McGuinness, C.; Lee, C.; Qi, M.; Tantawi, S. Coupling power into accelerating mode of a three-dimensional silicon woodpile photonic band-gap waveguide. *Phys. Rev. ST Accel. Beams* **2014**, *17*, 081301. [CrossRef]

6.　Yousefi, P.; McNeur, J.; Kozák, M.; Niedermayer, U.; Gannott, F.; Lohse, O.; Boine-Frankenheim, O.; Hommelhoff, P. Silicon dual pillar structure with a distributed Bragg reflector for dielectric laser accelerators: Design and fabrication. *Nucl. Instrum. Methods Phys. Res. Sect. Accel. Spectrometers Detect. Assoc. Equip.* **2018**, *909*, 221–223. [CrossRef]

7.　Crisp, S.; Ody, A.; Musumeci, P.; England, R.J. Resonant phase matching by oblique illumination of a dielectric laser accelerator. *Phys. Rev. Accel. Beams* **2021**, *24*, 121305. [CrossRef]

8.　Plettner, T.; Lu, P.P.; Byer, R.L. Proposed few-optical cycle laser-driven particle accelerator structure. *Phys. Rev. ST Accel. Beams* **2006**, *9*, 111301. [CrossRef]

9.　Peralta, E.A.; Colby, E.; England, R.J.; McGuinness, C.; Montazeri, B.; Soong, K.; Wu, Z.; Byer, R.L. Design, fabrication, and testing of a fused-silica dual-layer grating structure for direct laser acceleration of electrons. *AIP Conf. Proc.* **2012**, *1507*, 169–177. [CrossRef]

10.　Aimidula, A.; Bake, M.A.; Wan, F.; Xie, B.S.; Welsch, C.P.; Xia, G.; Mete, O.; Uesaka, M.; Matsumura, Y.; Yoshida, M.; et al. Numerically optimized structures for dielectric asymmetric dual-grating laser accelerators. *Phys. Plasmas* **2014**, *21*, 023110. [CrossRef]

11.　Wei, Y.; Ibison, M.; Xia, G.; Smith, J.D.A.; Welsch, C.P. Dual-grating dielectric accelerators driven by a pulse-front-tilted laser. *Appl. Opt.* **2017**, *56*, 8201–8206. [CrossRef] [PubMed]

12. Wei, Y.; Jamison, S.; Xia, G.; Hanahoe, K.; Li, Y.; Smith, J.D.A.; Welsch, C.P. Beam quality study for a grating-based dielectric laser-driven accelerator. *Phys. Plasmas* **2017**, *24*, 023102. [CrossRef]

13. Crisp, S.; Ody, A.; Musumeci, P. All Optical Chartacterization of a Dual Grating Accelerator Structure. In Proceedings of the 13th International Particle Accelerator Conference, Bangkok, Thailand, 12–17 June 2022. [CrossRef]

14. Black, D.S.; Zhao, Z.; Leedle, K.J.; Miao, Y.; Byer, R.L.; Fan, S.; Solgaard, O. Operating modes of dual-grating dielectric laser accelerators. *Phys. Rev. Accel. Beams* **2020**, *23*, 114001. [CrossRef]

15. Ody, A.; Crisp, S.; Musumeci, P.; Cesar, D.; England, R.J. SHarD: A beam dynamics simulation code for dielectric laser accelerators based on spatial harmonic field expansion. *Nucl. Instrum. Methods Phys. Res. Sect. Accel. Spectrometers Detect. Assoc. Equip.* **2021**, *1013*, 165635. [CrossRef]

16. Niedermayer, U.; Egenolf, T.; Boine-Frankenheim, O.; Hommelhoff, P. Alternating-Phase Focusing for Dielectric-Laser Acceleration. *Phys. Rev. Lett.* **2018**, *121*, 214801. [CrossRef] [PubMed]

17. Niedermayer, U.; Egenolf, T.; Boine-Frankenheim, O. Three Dimensional Alternating-Phase Focusing for Dielectric-Laser Electron Accelerators. *Phys. Rev. Lett.* **2020**, *125*, 164801. [CrossRef] [PubMed]

18. Naranjo, B.; Valloni, A.; Putterman, S.; Rosenzweig, J.B. Stable Charged-Particle Acceleration and Focusing in a Laser Accelerator Using Spatial Harmonics. *Phys. Rev. Lett.* **2012**, *109*, 164803. [CrossRef] [PubMed]

19. Shiloh, R.; Schönenberger, N.; Adiv, Y.; Ruimy, R.; Karnieli, A.; Hughes, T.; England, R.J.; Leedle, K.J.; Black, D.S.; Zhao, Z.; et al. Miniature light-driven nanophotonic electron acceleration and control. *Adv. Opt. Photon.* **2022**, *14*, 862–932. [CrossRef]

20. Peralta, E.A.; Soong, K.; England, R.J.; Colby, E.R.; Wu, Z.; Montazeri, B.; McGuinness, C.; McNeur, J.; Leedle, K.J.; Walz, D.; et al. Demonstration of electron acceleration in a laser-driven dielectric microstructure. *Nature* **2013**, *503*, 91–94. [CrossRef] [PubMed]